

An Investigation of PBO FRCM-Concrete Joint Behavior using a Three-Dimensional Numerical Approach

C. Carloni¹, T. D'Antino², L.H. Sneed³ and C. Pellegrino⁴

¹University of Bologna, Italy

²University of Patras, Greece

³Missouri University of Science and Technology
Rolla, United States of America

⁴University of Padova, Italy

Abstract

Fiber reinforced cementitious matrix (FRCM) composites represent an effective solution for strengthening and retrofitting existing reinforced concrete and masonry structures. The bond behavior between the FRCM composite and the support is of particular importance for the effectiveness of the strengthening intervention. In this paper the FRCM-concrete bond behavior is investigated using a three-dimensional numerical approach. The numerical model presented was calibrated and validated with a wide experimental programme previously conducted by the authors on PBO FRCM-concrete joints tested using the single-lap direct-shear test set-up. The results obtained from the numerical model of one of the specimens tested are shown in this paper. Good agreement between the experimental and numerical load responses and the strain profiles was obtained.

Keywords: strengthening, fiber reinforced cementitious matrix, finite element, debonding, shear stress, concrete.

1 Introduction

The growing need of strengthening and retrofitting existing structures is leading the civil engineering community toward the development of innovative high-performance materials. Among them, fiber reinforced polymer (FRP) composites represent a valid solution for strengthening existing reinforced concrete (RC) elements [1-3]. FRP composites are comprised of high strength fibers, typically carbon or glass fibers, and an organic matrix, usually epoxy resin, which provides bond between the composite and the substrate. The use of organic binder, however, is responsible for the poor properties of FRP composites at temperatures close or higher than the matrix glass transition temperature [4]. Furthermore, the organic matrix suffers from degradation when exposed to UV radiation and does not allow the vapor permeability of the substrate. A promising alternative to the use of organic

matrices is represented by inorganic matrices. Inorganic cement-based matrices have raised particular interest because of their compatibility with the substrate. Fiber reinforced composites that employ cement-based matrices are usually referred to as fiber reinforced cementitious matrix (FRCM) composites. FRCM composites are comprised of high strength fibers organized in discrete bundles to improve the matrix-fiber bond. Bundles spacing, fiber material, and matrix type can be varied leading to different composite properties and behavior. FRCM composites have been shown to be effective in strengthening existing RC and masonry elements in flexure [5-8] and shear [9-11] and to confine axially loaded elements [12-14]. Although FRCM composites have been applied in a limited number of strengthening and retrofitting applications of RC and masonry structures in practice [15], they are still in their infancy, and a limited number of studies are available in the literature. Failure of FRCM-strengthened concrete elements is generally reported to be debonding of the FRCM composite [16,17]. Debonding may occur at the matrix-fiber interface, at the composite-concrete interface, or within the concrete substrate depending on the materials employed [18] and on the strengthening configuration [19]. The study of the bond characteristics of FRCM-concrete joints is crucial to understand the behavior of FRCM-strengthened elements and to develop reliable design models.

This paper presents a three-dimensional numerical model developed to describe the bond behavior of the FRCM-concrete interface. The numerical approach adopted was calibrated and validated by the experimental results previously obtained by the authors on FRCM-concrete joints tested with a single-lap direct-shear set-up [20-22]. The numerical model of one of the specimens tested is shown in this paper. The shear stress-slip relationship used to define the matrix-fiber interfacial bond behavior in the numerical model was obtained from the strain profiles measured experimentally on the specimen considered.

2 Experimental programme

The experimental research programme included 123 specimens with six different composite bonded lengths ℓ and four different composite bonded widths b_1 . The experimental program and results are presented in detail in [20-22] and are summarized in this section for comparison with the numerical simulation presented in the next section.

2.1 Materials and test set-up

The FRCM-concrete joints were comprised of one layer of a bidirectional polyparaphenylene benzobisoxazole (PBO) fiber net embedded within an inorganic polymer-modified cementitious matrix. The fiber net was comprised of longitudinal and transversal PBO fiber bundles spaced at 10 mm and 20 mm, respectively. The thickness and width of a single PBO fiber bundle were $t^*=0.092$ mm and $b^*=5$ mm, respectively. The mechanical characteristics of the PBO fibers were determined by means of tensile tests of PBO fiber net specimens with different widths. The average

measured tensile strength, ultimate strain, and elastic modulus were 3014 MPa (CoV = 0.068), 0.0145 (CoV = 0.104), and 206 GPa (CoV = 0.065), respectively [23]. The compressive and splitting tensile strength of the matrix were obtained from a minimum of two 50 mm × 100 mm cylinders cast from each batch used to construct the composite strips and were 28.4 MPa (CoV=0.092) and 3.5 MPa (CoV=0.231), respectively [24,25]. Two different concrete prisms were used, both with a 125 × 125 mm cross-section but different lengths ($L=375$ or 510 mm). The concrete prisms were characterized by means of compressive and splitting tests of 100 mm × 200 mm concrete cylinders [24,25] cast from the same batches used to construct the prisms. The average compressive and splitting strength of prisms with $L=375$ mm were 42.5 MPa (CoV=0.013) and 3.4 MPa (CoV= 0.113), respectively, whereas for prisms with $L=510$ mm they were 33.5 MPa (CoV=0.085) and 3.0 MPa (CoV= 0.042), respectively.

The specimens were tested using a single-lap direct shear test set-up, where a single composite strip was bonded to the surface of a concrete block (prism). The classical push-pull configuration was adopted where the fibers were pulled while the concrete block was restrained (Figure 1). The surface of the concrete block onto which the FRCM composite was applied was sandblasted to improve the bond between the matrix and the substrate. Fibers were embedded within the matrix only along the bonded length, whereas they were left bare outside the bonded length.

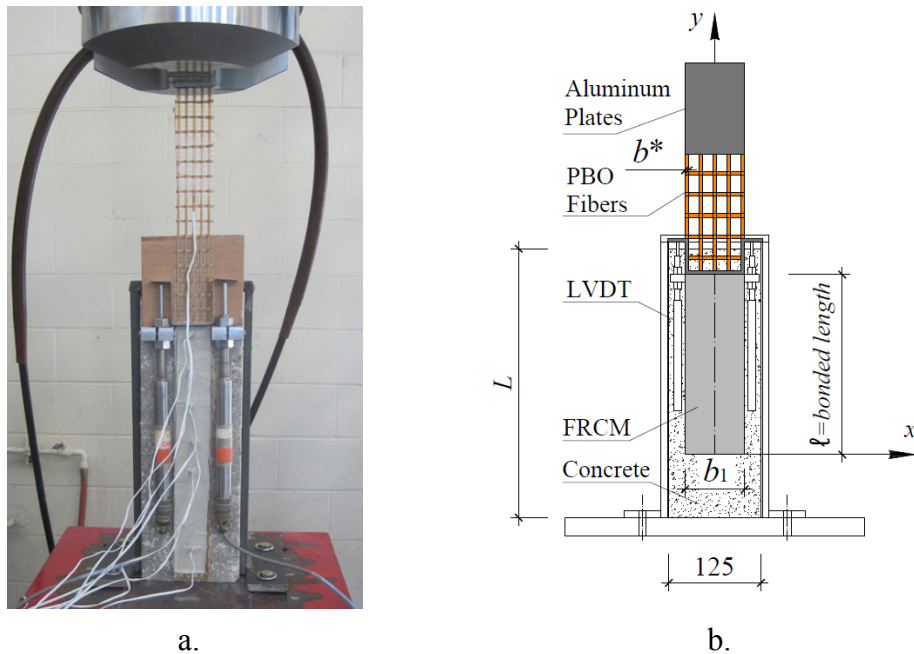


Figure 1: a) Specimen DS_330_43_S_5. b) Test set-up (units in mm)

Tests were conducted in displacement control using a close-loop servo-hydraulic universal testing machine. Aluminum plates were bonded to the bare fiber end to improve gripping with the machine. Two LVDTs were mounted on concrete on the sides of the composite strip just beyond the bonded area and reacted off of a thin

aluminum Ω -shaped plate bonded at the beginning of the bare fibers (Figure 1). The average measurement of the two LVDTs, termed global slip g , was used to control the tests that were conducted at a constant rate of 0.00084 mm/s.

The central fiber bundle of some specimens was equipped with uniaxial electrical resistance strain gauges mounted along the composite bonded length to investigate the stress transfer mechanism that characterizes the matrix-fiber interface.

2.2 Experimental results

The failure of all specimens was debonding at the matrix-fiber interface and was characterized by considerable slippage between the fibers and the matrix. Based on the information inferred from the results of the experimental programme, the authors put forward the idealized load response of PBO FRCM-concrete joints shown in Figure 2. It should be noted that the idealized load response depicted in Figure 2 is valid when the bonded length is longer than the effective bond length l_{eff} , i.e. the minimum length needed to fully develop the stress-transfer mechanism [21,22]. After a linear branch, up to point A in Figure 2, the applied load – global slip behavior is characterized by a non-linear response. When the applied load attains the load-carrying capacity P_{deb} (point B in Figure 2) the stress-transfer mechanism is fully established, and the fibers start to debond from the embedding matrix. Further increase of the global slip g after the onset of debonding results in an increase of the applied load due to the presence of friction (interlocking) between single fiber filaments and between fibers and matrix in the debonded region. After the applied load reaches the peak load P^* (point C in Figure 2) further increase of the global slip results in a decrease of the applied load until the constant load P_f due to friction is attained (point D in Figure 2).

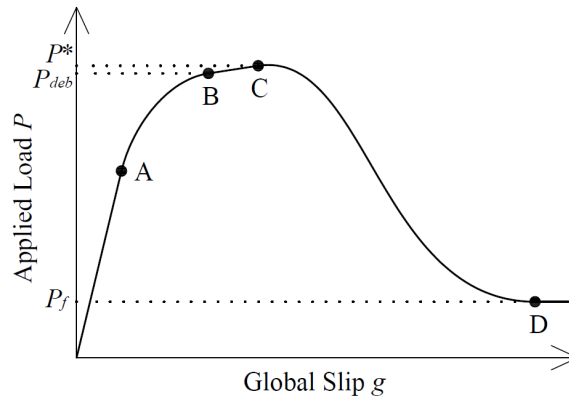


Figure 2: Idealized applied load – global slip response

The fiber strains measured along the composite bonded length of specimens equipped with strain gauges were employed to determine the shear stress τ_{xy} - slip s relationship through a fracture mechanics approach previously applied to FRP-concrete joints and extended to FRCM-concrete joints [21]. Since the fibers are

embedded within the matrix, an internal and an external matrix layer-fiber interface exists, where internal and external correspond to the matrix layers applied directly to the substrate and over the fiber net, respectively. In general, the bond behavior of the internal matrix layer-fiber interface may be different from the bond behavior of the external matrix layer-fiber interface. As a first attempt to determine the $\tau_{zy} - s$ relationship that characterizes PBO FRCM-concrete joints with one fiber layer, it was assumed that the bond behavior of the internal and external matrix layer-fiber interfaces is equal. The strain profiles obtained experimentally along the bonded length were differentiated and integrated to obtain the shear stress τ_{zy} and slip s according to Equations (1) and (2), respectively:

$$\tau_{zy} = \frac{1}{2} Et^* \frac{d\varepsilon_{yy}}{dy} \quad (1)$$

$$s = \int_0^y \varepsilon_{yy} dy \quad (2)$$

where ε_{yy} is the measured strain, E is the fiber elastic modulus, and y is the location along the bonded length of composite (see Figure 1b). It should be noted that Equations (1) and (2) provide the shear stress and slip of one matrix-fiber interface. The integral of the $\tau_{zy} - s$ curve obtained when the applied load is equal to the FRCM-concrete joint load-carrying capacity, i.e. the debonding load P_{deb} (point B in Figure 2), represents the fracture energy G_F associated with each matrix-fiber interface:

$$G_F = \int_0^{s_f} \tau_{zy} ds \quad (3)$$

where s_f is the slip corresponding to the complete debonding of the fibers from the matrix.

3 Numerical simulation

The results obtained from one of the specimens equipped with strain gauges mounted to the longitudinal fibers of the central bundle, specimen DS_330_43_S_5, were modelled using the numerical software Abaqus [26]. The numerical model and the results are presented in this section.

3.1 Numerical approach adopted

As a first attempt to reproduce the observed behavior of the FRCM-concrete joint, both the PBO fibers and the matrix layers were specified as homogeneous isotropic linear elastic materials. The matrix-fiber interfaces were modeled by means of a master-slave contact interaction that follows a cohesive damage law. The contact

surfaces between the matrix and the sides of the fiber bundle, each having an area equal to 0.092 mm^2 per unit length, was disregarded.

A $\tau_{zy} - s$ curve obtained from an experimental test was employed to determine the input values for the shear stress – slip relationship between the master and slave surfaces. The surface-based cohesive behavior available in Abaqus was used to model the linear elastic branch of the $\tau_{zy} - s$ relationship whereas the non-linear branch was modeled introducing a damage variable that simulates the interface degradation. The surface-based cohesive behavior is expressed by a linear elastic traction-separation model that relates the normal and shear stresses to the normal and shear separations across the interface by means of an elastic constitutive matrix \mathbf{K} [26]. The cohesive behavior can be expressed as:

$$\mathbf{t} = \begin{Bmatrix} t_n \\ t_s \\ t_t \end{Bmatrix} = \begin{bmatrix} K_{nn} & K_{ns} & K_{nt} \\ K_{sn} & K_{ss} & K_{st} \\ K_{tn} & K_{ts} & K_{tt} \end{bmatrix} \begin{Bmatrix} \delta_n \\ \delta_s \\ \delta_t \end{Bmatrix} = \mathbf{K}\boldsymbol{\delta} \quad (4)$$

where \mathbf{t} is the traction vector of normal component t_n and shear components t_s and t_t , and δ_n , δ_s , and δ_t are the corresponding components of the separation vector $\boldsymbol{\delta}$. The cohesive behavior contributes to the normal behavior only when a slave node is open, i.e. when it is not in contact with the master surface, whereas when a slave node is closed, i.e. when it is in contact with the master surface, the contact pressure is directly transmitted [26]. In order to model the non-linear branch of the $\tau_{zy} - s$ relationship, a damage criterion was introduced into the linear elastic cohesive law, which allows for modeling the degradation and failure of the bond between the master and slave surfaces. The onset of damage was specified by defining the limit values t_n^0 , t_s^0 , and t_t^0 of the traction vector components beyond which the damage variable d reduces the corresponding stress t_n , t_s , and t_t , respectively:

$$t_i = \begin{cases} (1-d) \cdot \bar{t}_i & \text{if } \bar{t}_i > t_i^0 \\ \bar{t}_i & \text{if } \bar{t}_i \leq t_i^0 \end{cases} \quad (5)$$

where t_i is the i -th component of the traction vector, and \bar{t}_i is the corresponding elastic component computed using the cohesive material law expressed by Equation (4). The damage evolution law is then specified by defining the values of the damage variable with respect to the non-dimensional plastic displacement $\delta_s = \delta_i^u - \delta_i^0$, which is the difference between the effective separation at complete failure δ_i^u and the effective separation at the onset of damage δ_i^0 [26].

Since the experimental investigation of specimens with different bonded widths showed that a global width effect does not exist for the entire composite width [21],

only one fiber bundle was modelled, and the results obtained were multiplied by the number of bundles present in the corresponding experimental test.

3.2 Finite element model

In this study the experimental results obtained for specimen DS_330_43_S_5 [21] were reproduced numerically. Specimen DS_330_43_S_5 had a bonded length and bonded width of 330 mm and 43 mm, respectively, and included 5 longitudinal fiber bundles. It should be noted that at the peak load P^* , the applied load was not evenly distributed among the different bundles in specimen DS_330_43_S_5 [22]. However, since the applied load was evenly distributed among the fiber bundles up to the onset of debonding, the specimen was considered for the numerical analysis and good results were obtained, as discussed below.

The numerical model developed, termed DS_330_43_S_5_num and shown in Figure 3, was comprised of a single longitudinal bundle of PBO fiber embedded within two layers of matrix.

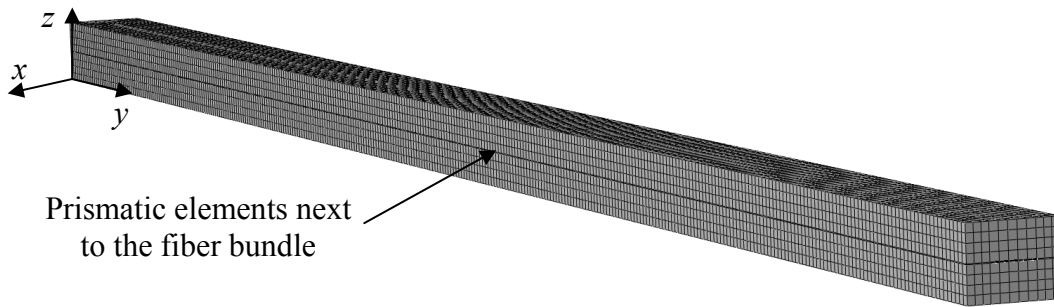


Figure 3: Geometry and mesh of model DS_330_43_S_5_num

The transversal fiber bundles were not included in the numerical model since the fracture mechanics approach used to define the model parameters was determined without taking into account the presence of the transversal fiber bundles [22]. Each of the two matrix layers had a length, thickness, and width of 330 mm, 4 mm, and 10 mm, respectively, and was implemented in the numerical model as a continuum body with the fiber bundle placed in a through-length hole at the center of the body cross-section. The fiber bundle had the same length as the matrix layers and a 0.092 mm-thick \times 5 mm-wide rectangular cross-section. Since the $\tau_{zy} - s$ curve was obtained from the fracture mechanics approach assuming that the matrix deformation is negligible [22], the matrix layers were specified as rigid bodies by setting their elastic modulus E_m equal to 1000 GPa. The elastic modulus of the fibers was $E=206$ GPa, whereas the value of Poisson's ratio of the matrix and the fibers was 0.2 [27] and 0.3 [28], respectively. The concrete substrate, whose deformation was assumed to be negligible with respect to the matrix and fiber deformation, was not modeled, and the internal matrix layer surface was restrained from any movement. A displacement of 4 mm in y direction was applied to one end

of the fiber bundle and was attained through steps whose amplitude was automatically determined by the software to obtain the most rapid convergence.

The fiber-matrix internal and external interfaces were defined by a master-slave contact, where the matrix represented the master, and the fiber represented the slave. The $\tau_{zy} - s$ curves obtained from the fracture mechanics approach applied to specimen DS_330_43_S_5 were used to determine the shear parameters needed to define the damage cohesive contact law that controls the master-slave interaction. Figure 4 shows the shear stress τ_{zy} versus slip s relationship corresponding to the onset of debonding (point B5 in Figure 5), obtained assuming that the bond behavior of the internal and external matrix layers was equal, which was used to determine the components of the elastic constitutive matrix \mathbf{K} , the damage variable d , and the corresponding non-dimensional plastic displacement δ_s . Since the $\tau_{zy} - s$ curve is defined for y direction, \mathbf{K} is fully defined by K_{yy} , which corresponds to the slope of the elastic branch of the $\tau_{zy} - s$ curve. When damage occurs the $\tau_{zy} - s$ curve deviates from the linear behavior defined by K_{yy} . The shear stress corresponding to the onset of damage, τ^0 , was defined by analyzing the elastic branch of the $\tau_{zy} - s$ and was found equal to 0.5 MPa. The $\tau_{zy} - s$ curve computed from the experimental strain at point B5 and the $\tau_{zy} - s$ curve obtained from the numerical model at point B_num (Figure 5), which was directly provided by the software, are depicted in Figure 4.

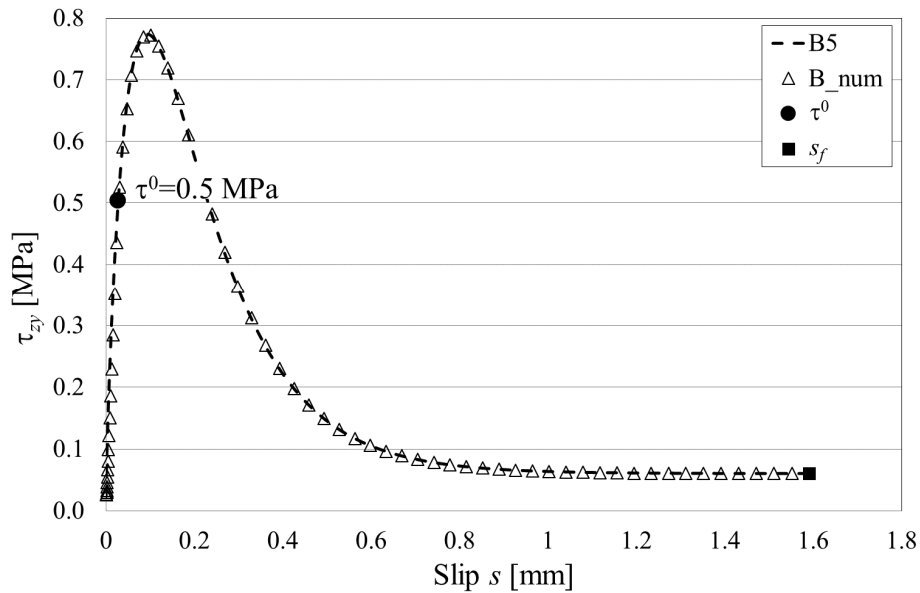


Figure 4: Comparison between the experimental and numerical shear stress τ_{zy} vs. slip s curves of point B5 (Figure 5) and B_num

Both the fiber bundle and the matrix were modeled using eight-node linear brick elements. Different mesh sizes were employed to study the influence of the model discretization. The mesh size adopted and herein described was found to be the best model discretization since it provided accurate results with a short solution time. The matrix was discretized into 26424 cube elements with an average edge of 0.4 mm, except for the prismatic elements placed next to fiber bundle lateral surfaces (Figure 3). The fiber bundle was discretized into three brick elements along the bundle thickness with a size of approximately $0.5 \times 0.5 \times 0.03$ mm in x , y , and z directions, respectively. The total number of brick elements in the fiber bundle was 19800 (Figure 7).

3.3 Numerical results

The results obtained from the numerical model, which were multiplied by the number of bundles included in specimen DS_330_43_S_5, are in good agreement with the experimental results. Figure 5 shows the comparison between the load response of specimen DS_330_43_S_5 and the load response of the numerical model DS_330_43_S_5_num.

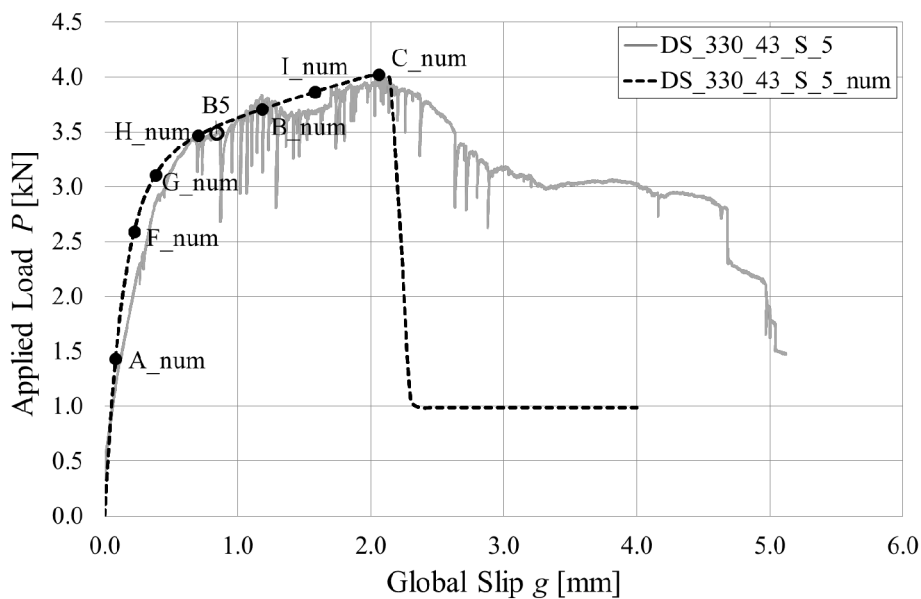


Figure 5: Load responses of specimen DS_330_43_S_5 and model DS_330_43_S_5_num

Point A_num, B_num, and C_num of the numerical load response depicted in Figure 5 correspond to point A, B, and C, respectively, of the idealized load response of Figure 2. The numerical load response is linear until point A_num, and it becomes non-linear after point A_num. At point B_num the stress-transfer mechanism between the fibers and the matrix is fully established, and the area under the $\tau_{xy} - s$ curve defines the fracture energy of the interface. After point B_num the

applied load increases due to the presence of friction (interlocking) between fiber filaments and between fibers and matrix. It should be noted that the contribution of the friction between fiber filaments is included in the $\tau_{zy} - s$ relationship of the matrix-fiber interfaces.

After attaining the peak load P^* , which corresponds to the applied load value at point C_num, the stress-transfer mechanism is no longer fully established, and the applied load decreases until the fiber strip is completely debonded from the matrix (point D in Figure 2).

The decreasing branch of the load response, which in the experimental tests is characterized by a softening behavior, appears to be brittle in the numerical simulation. This particular behavior of the numerical response is mainly attributed to the solution method adopted. The analysis was run using a full Newton solution technique, which is not able to describe complex non-linear phenomena, such as the softening behavior that follows the peak load. Furthermore, the analysis was carried out allowing the software to automatically determine the optimum displacement increment to obtain the most rapid convergence, which results in a rapid drop from the peak load to the load associated with pure friction (interlocking). It should be noted, however, that the post peak behavior is characterized by complex phenomena that cannot be described by the $\tau_{zy} - s$ relationship obtained when the stress-transfer mechanism is fully established. Further analysis performed using a different solution method and by fixing the displacement increment might better reproduce the post-peak softening behavior of FRCM-concrete joints and will be carried out by the authors in the future.

Good agreement between the strain profiles measured experimentally at point B5 (Figure 5) and obtained from the numerical model at point B_num (Figure 5) was obtained, as can be observed in Figure 6.

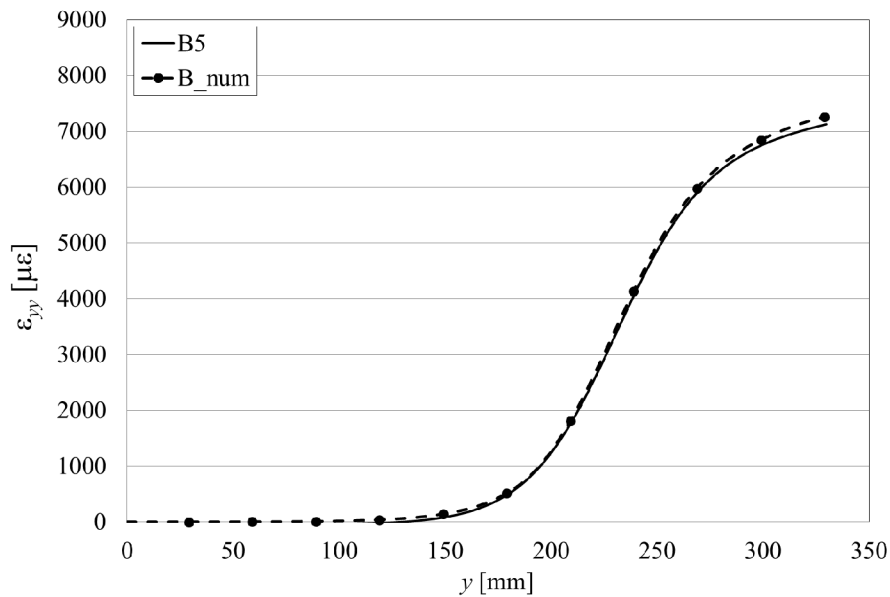


Figure 6: Comparison between strain profiles measured experimentally at point B5 and obtained from the numerical model at point B_num (Figure 5)

The strain profiles obtained from the numerical model and corresponding to points of the numerical load response of Figure 5 are depicted in Figure 7. Figure 7 can be used to study the evolution of the strain along the bonded length, especially for high values of the applied load where measuring the fiber strain is challenging [21].

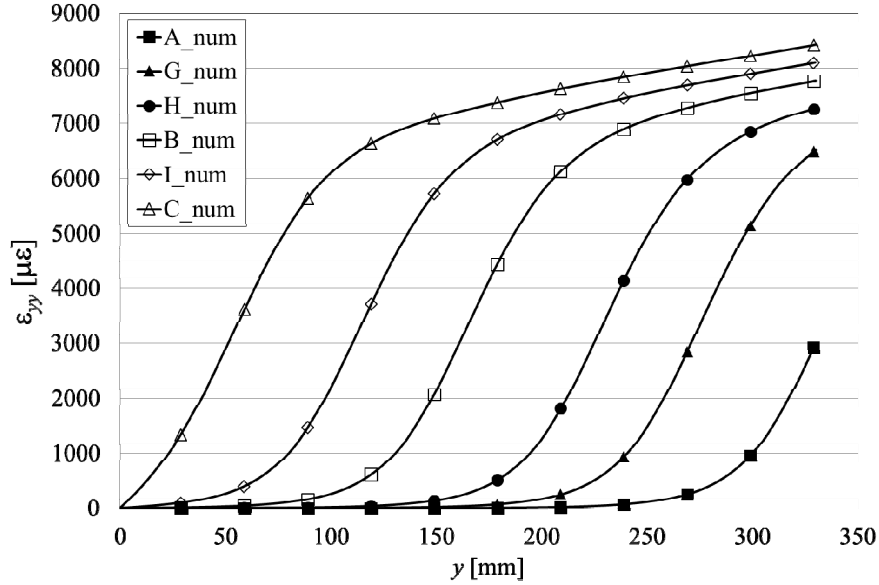


Figure 7: Strain profiles obtained from the numerical model for points of the numerical load response (Figure 5)

The propagation of debonding along the matrix-fiber interface can also be observed from the contours of the shear stress τ_{zy} , which are depicted in Figure 8 for different points of the numerical load response. For point A_num (Figure 8a) the stress-transfer mechanism is not fully established, as it can be seen by the fact that the shear stress τ_{zy} has a maximum value of approximately 0.76 MPa, which is lower than the maximum stress of the experimental τ_{zy-s} of approximately 0.77 MPa (Figures 7b-f). After point A_num (Figures 7b-f) the shear stress τ_{zy} attains its maximum value and, from point B_num (Figures 7d), the stress-transfer mechanism is fully established. After point B_num the portion of the bonded length involved in the stress-transfer mechanism translates toward the free end with increasing global slip g .

The use of a three-dimensional model allowed for investigating the distribution of the strain across the width of the longitudinal fiber bundle. In case of FRP-concrete joints the strain distribution across the composite plate width follows a parabolic-type shape with the maximum value in the middle of the width [29]. In case of FRCM-concrete joints, the numerical model employed in this study shows that the strain is constant across the width of the fiber bundle. However, further and more sophisticated numerical analyses will be carried out to study the effect of the different impregnation of the outer and core fiber filaments on the strain distribution across the bundle width [30].

software Abaqus. The results of single-lap direct-shear tests conducted on FRCM-concrete joints comprised of one layer of PBO fiber net embedded within two layers of cementitious matrix were simulated. The shear stress-slip relationship obtained from an experimental test was used to define the matrix-fiber contact behavior of the numerical model using a damage cohesive contact law.

The numerical results obtained are in good agreement with the experimental observations. The following conclusions can be drawn:

- The numerical load response well simulates the initial elastic behavior, followed by the non-linear branch corresponding to microdamage of the matrix-fiber interfaces. After the onset of debonding the numerical load response increases linearly due to friction between fiber filaments and between fiber and matrix, as observed from the experimental results.
- The numerical strain profiles along the fiber strips well reproduce the strain profiles observed experimentally and can be used to determine the value of the effective bond length of PBO FRCM composites.
- The use of a simplified numerical model that includes a single fiber bundle and the embedding matrix, the results of which were multiplied by the number of bundles of the corresponding experimental test, was shown to be accurate in simulating the response of the specimen considered.
- The use of a three-dimensional model allowed for studying the behavior of the fiber strain, which was observed to be constant across the bundle width.

References

- [1] T.C. Triantafillou, N. Plevris, “Strengthening of RC beams with epoxy-bonded fibre-composite materials”, *Materials and Structures*, 25, 201-211, 1992.
- [2] C. Pellegrino, C. Modena, “FRP shear strengthening of RC beams: experimental study and analytical modelling”, *ACI Structural Journal*, 103(5), 720-728, 2006.
- [3] Y. Yang, L.H. Sneed, A. Morgan, M.S. Saiidi, A. Belarbi, “Repair of RC bridge columns with interlocking spirals and fractured longitudinal bars - An experimental study”, *Construction and Building Materials*, 78, 405-420, 2015.
- [4] E. Nigro, G. Cefarelli, A. Bilotta, G. Manfredi, E. Cosenza, “Guidelines for flexural resistance of FRP reinforced concrete slabs and beams in fire”, *Composite Part B: Engineering*, 58, 103-112, 2014.
- [5] A. D’Ambrisi, F. Focacci, “Flexural Strengthening of RC beams with Cement Based Composites”, *Journal of Composites for Construction*, ASCE, 15(2), 707-720, 2011.
- [6] S. Hashemi, R. Al-Mahaidi, “Experimental and finite element analysis of flexural behavior of FRP-strengthened RC beams using cement-based adhesives”, *Construction and Building Materials*, 26, 268-273, 2012.
- [7] L. Ombres, “Debonding Analysis of Reinforced Concrete Beams Strengthened with Fibre Reinforced Cementitious Mortar”, *Engineering Fracture Mechanics*, 81, 94-109, 2012.

- [8] C. Pellegrino, T. D'Antino, "Experimental behaviour of existing precast prestressed reinforced concrete elements strengthened with cementitious composites", *Composite Part B: Engineering*, 55, 31-40, 2013.
- [9] T. Blanksvärd, B. Täljsten, A. Carolin, "Shear strengthening of concrete structures with the use of mineral-based composites", *Journal of Composites for Construction*, ASCE, 13(1), 25-34, 2009.
- [10] E. Tzoura, T.C. Triantafillou, "Shear strengthening of reinforced concrete T-beams under cyclic loading with TRM or FRP jackets", *Materials and Structures*, 2014, DOI 10.1617/s11527-014-0470-9.
- [11] L. Ombres, "Structural performance of reinforced concrete beams strengthened in shear with a cement based fiber composite material", *Composite Structures*, 122, 316-329, 2015.
- [12] A. Peled, "Confinement of damaged and nondamaged structural concrete with FRP and TRC sleeves. *Journal of Composites for Construction*, ASCE, 11(5), 514-22, 2007.
- [13] D.A. Bournas, T.C. Triantafillou, K. Zygouris, F. Stavropoulos, "Textile-reinforced mortar versus FRP jacketing in seismic retrofitting of RC columns with continuous or lap-spliced deformed bars", *Journal of Composites for Construction*, ASCE, 13(5), 360-371, 2009.
- [14] C. Carloni, C. Mazzotti, M. Savoia, K.V. Subramaniam, "Confinement of masonry columns with PBO FRCM composites", *Key Engineering Materials*, 624, 644-651, 2015.
- [15] A. D'Ambrisi, F. Focacci, L. Raimondo, V. Alecci, M. De Stefano, "Carbon FRCM materials for structural upgrade of masonry arch and road bridges", *Composite Part B: Engineering*, 2015, DOI: 10.1016/j.compositesb.2015.01.024.
- [16] A. D'Ambrisi, L. Feo, F. Focacci, "Experimental analysis on bond between PBO-FRCM strengthening materials and concrete", *Composite Part B: Engineering*, 44(1), 524-532, 2013.
- [17] C.T.M. Tran, B. Stitmannathum, T. Ueda. "Investigation of the bond behavior between PBO-FRCM strengthening material and concrete", *Journal of Advanced Concrete Technology*, 12, 545-557, 2014.
- [18] T. D'Antino, C. Pellegrino, C. Carloni, L.H. Sneed, G.Giacomin. "Experimental analysis of the bond behavior of glass, carbon, and steel FRCM composites", *Key Engineering Materials*, 624, 371-378, 2015.
- [19] S. Babaeidarabad, G. Loreto, Nanni A, "Flexural Strengthening of RC Beams with an Externally Bonded Fabric-Reinforced Cementitious Matrix", *Journal of Composites for Construction*, 18(5), 2014, DOI: 10.1061/(ASCE)CC.1943-5614.0000473.
- [20] L.H. Sneed, T. D'Antino, C. Carloni, "Investigation of bond behavior of PBO fiber-reinforced cementitious matrix composite-concrete interface", *ACI Material Journal*, 111(5), 569-580, 2014.
- [21] T. D'Antino, C. Carloni, L.H. Sneed, C. Pellegrino, "Matrix-fiber bond behavior in PBO FRCM composites: A Fracture Mechanics Approach", *Engineering Fracture Mechanics*, 117, 94-111, 2014.

- [22] C. Carloni, T. D'Antino, L.H. Sneed, C. Pellegrino, "Role of the matrix layers in the stress-transfer mechanism of FRCM composites bonded to a concrete substrate", *Journal of Engineering Mechanics*, ASCE, 2014, DOI: 10.1061/(ASCE)EM.1943-7889.0000883.
- [23] T. D'Antino, L.H. Sneed, C. Carloni, C. Pellegrino, "Bond behavior of the FRCM-concrete interface", In *Proc. of the 11th Int. Symp. on Fiber Reinforced Polymers for Reinforced Concrete Structures*, J. Barros and J. Sena-Cruz eds., Univ. Minho, Guimaraes, Portugal, 2013.
- [24] ASTM, "Standard test method for compressive strength for cylindrical concrete specimens", C39/C39M-12 ASTM International, 2011.
- [25] ASTM, "Standard test method for splitting tensile strength of cylindrical concrete specimens", C496/C496M ASTM International, 2011.
- [26] Simulia, "Abaqus 6.10 Extended Functionality Online Documentation" (generated September 29, 2010).
- [27] Fib Task Group 9.3, "Externally bonded FRP reinforcement for RC structures", International Federation for Structural Concrete, 2001, Lausanne, Switzerland.
- [28] Y.K. Huang, P.H. Frings, E. Hennes, "Mechanical properties of Zylon/epoxy composite", *Composite Part B: Engineering*, 33(2), 109-115, 2002.
- [29] V. Salomoni, G. Mazzucco, C. Pellegrino, C. Majorana, "Three-dimensional modelling of bond behaviour between concrete and FRP reinforcement", *Engineering Computations*, 28(1), 5-29, 2011.
- [30] B. Banholzer, "Bond behavior of multi-filament yarn embedded in a cementitious matrix", Ph.D. thesis, Rheinisch-Westfälische Technische Hochschule (RETH) Aachen Univ., Aachen, Germany, 2004.